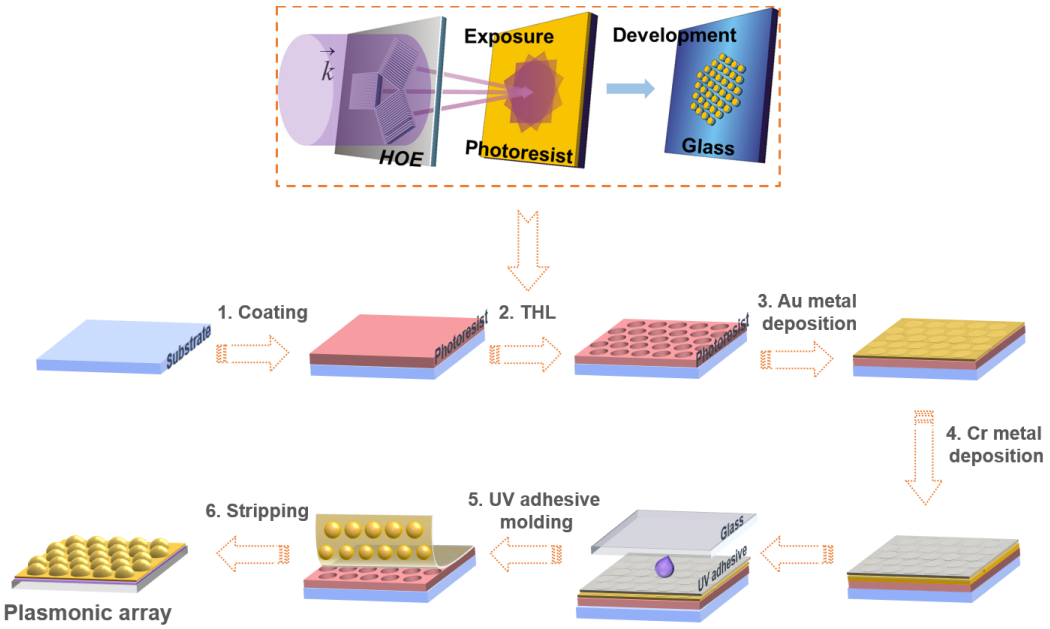

Extended Data Fig. 1 | Schematic of plasmonic nanoparticle array fabricated using UV holographic lithography.

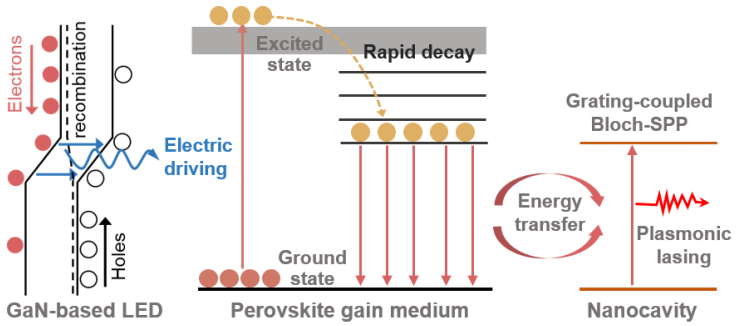

Extended Data Fig. 2 | The operating principle of the lasing system. Including the LED electroluminescence drive unit (left), the energy level diagram of the Ca^{2+}-$CsPbI_3$ gain material (center), and energy transfer (right) between the gain and the hexagonal plasmonic nanocavity.

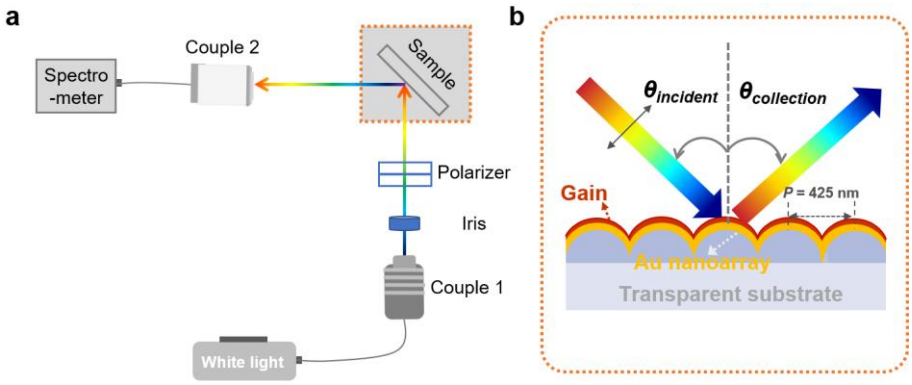

Extended Data Fig. 3 | Schematic of angle-resolved detection. a, Optical path diagram: A halogen lamp serves as the incident light source. The optical signal is introduced into coupler 1 via an optical fiber, transmitted through an optical cable, and incident onto the sample surface after passing through a fixed p-polarizer. The reflected signal is collected by coupler 2 and transmitted to a compact CCD spectrometer for analysis. The experiment employs a gold film as the background. **b,** Localized enlargement schematic of the sample area: demonstrates the localized state of perovskite placed on the sample surface.

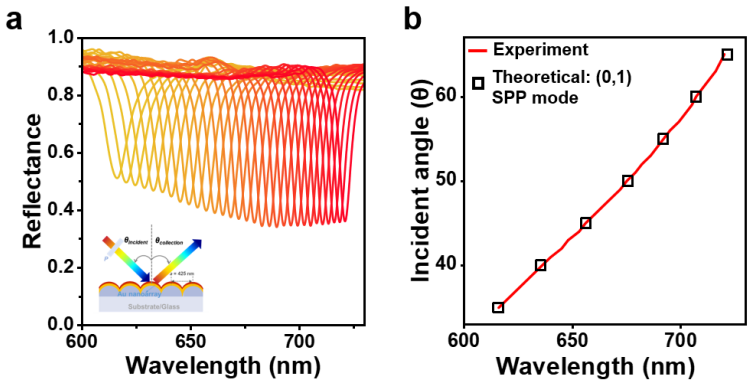

Extended Data Fig. 4 | Characterization of surface plasmon modes. a, Angle-resolved reflectance spectra of gold plasmonic array over an incident angle range of 35° to 63°. Insert: Schematic of the measurement setup. **b,** Relationship between the resonance wavelength of surface plasmon modes as a function of incident angle, measured experimentally (red line) versus theoretically predicted (squares).

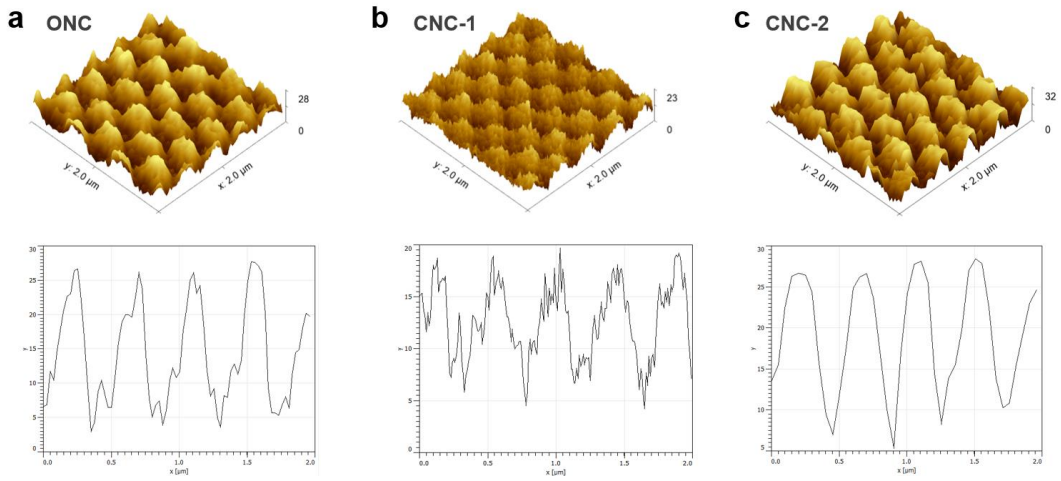

Extended Data Fig. 5 | Atomic force microscopy (AFM) images of three metal nanoparticle arrays with tunable morphologies achieved through precise control.

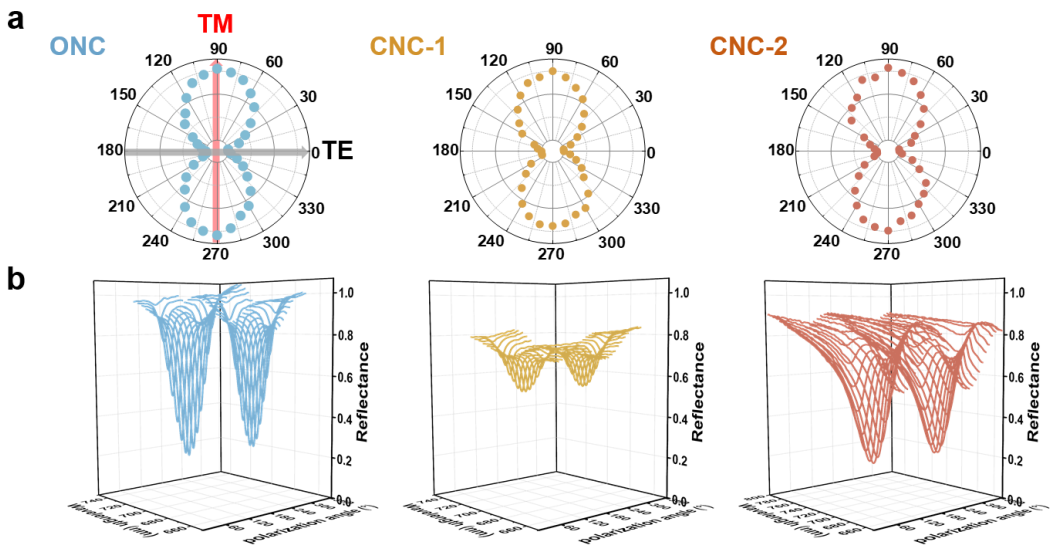

Extended Data Fig. 6 | Polarization characteristics of ONC、CNC-1 and CNC-2 surface plasmon resonance (SPR) reflectance spectra. a, Polarized polar coordinate diagram (The TM and TE modes corresponding to the plasmonic array structure are labeled in the ONC polarization diagram). **b,** Polarized spectra diagram.

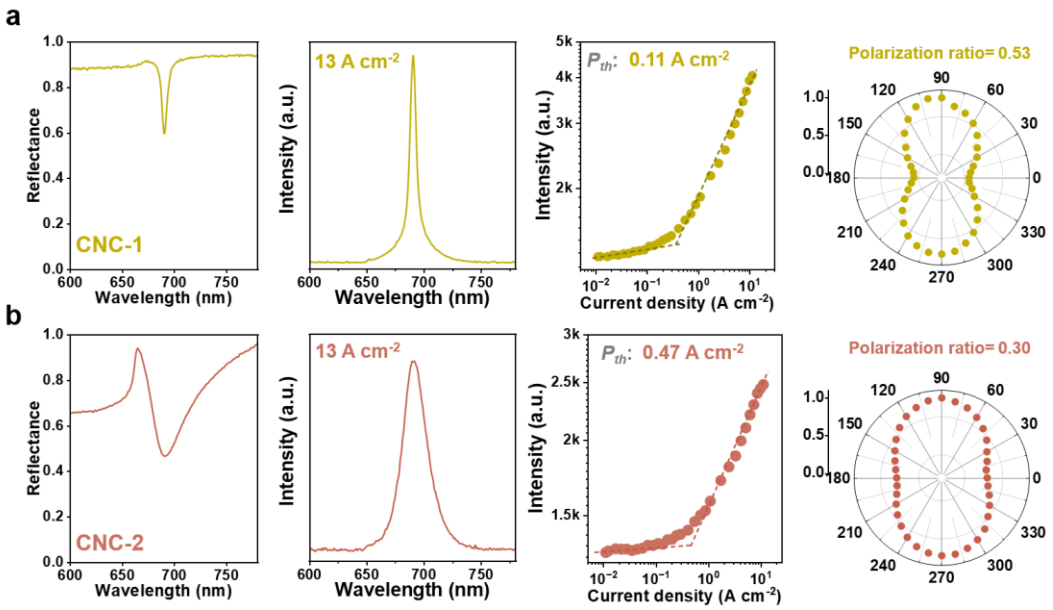

Extended Data Fig. 7 | The performance of the two control nanocavities (CNC-1 and CNC-2).

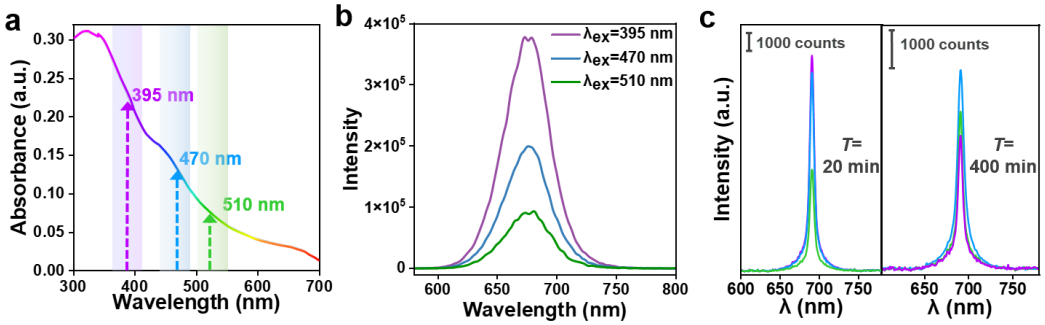

Extended Data Fig. 8 | Spectral characterization and comparison of Ca^{2+}-$CsPbI_3$ gain materials under different excitation wavelengths. a, Absorption spectrum. **b,** PL spectrum. **c,** After continuous irradiation for 20 min and 400 min electro-driven lasing spectrum.

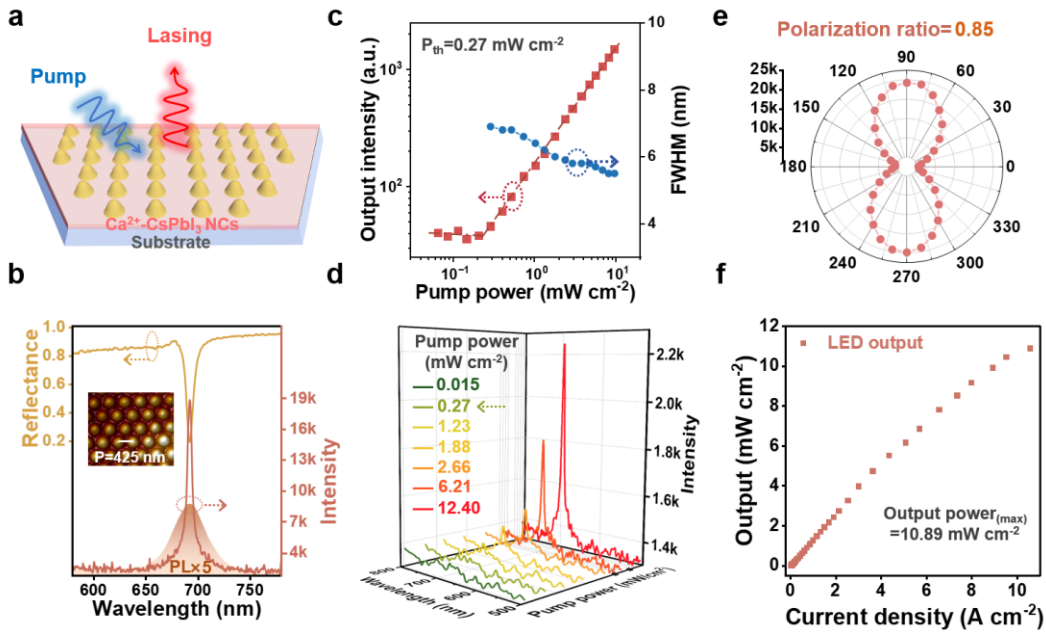

Extended Data Fig. 9 | Characterization of perovskite in plasmonic cavities under optical pumping. a, Experimental setup schematic, employing a 405 nmCW laser as the pump source. **b,** SPR mode (yellow curve) of the plasmonic cavity, perovskite photoluminescence spectrum (filled area), and plasmonic laser emission spectrum (brown curve); inset shows AFM topography of the plasmonic cavity. **c,** Relationship between output optical power intensity and FWHM versus pump intensity, showing a distinct laser threshold transition at approximately 0.27 mW·cm^{-2}. **d,** Emission spectra at different pump intensities. **e,** Polar coordinate diagram of laser polarization with a polarization ratio of 0.79. **f,** Growth curve of LED output power versus current density, with a maximum output power of 10.89 mW·cm^{-2}.

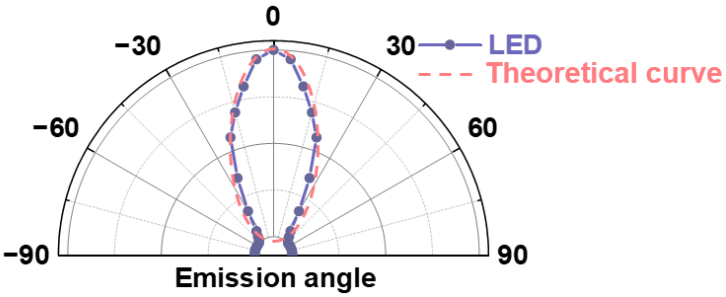

Extended Data Fig. 10 | Emission angle dependence of 470 nm LED driver sources.